

# Modeling thermal effects and polarization competition in vertical-cavity surface-emitting lasers

C. Masoller<sup>a</sup> and M. S. Torre<sup>b</sup>

<sup>a</sup>*Departament de Física i Enginyeria Nuclear, Universitat Politècnica de Catalunya, Colom 11, E-08222 Terrassa, Barcelona, Spain;* <sup>b</sup>*Instituto de Física "Arroyo Seco", U.N.C.P.B.A, Pinto 399 (7000), Tandil, Argentina*  
[crisrina.masoller@upc.edu](mailto:crisrina.masoller@upc.edu), [marita@exa.unicen.edu.ar](mailto:marita@exa.unicen.edu.ar)

**Abstract:** We analyze the influence of thermal effects on the polarization-resolved light-current (LI) characteristics of vertical-cavity surface-emitting lasers (VCSELs). We use a model that is an extension of the spin-flip model incorporating material gain that is frequency and temperature dependent, and a rate equation for the temperature of the active region, which takes into account decay to a fixed substrate temperature, Joule heating and nonradiative recombination heating. The model also incorporates the red shift for increasing temperature of the gain curve and of the cavity resonance. The temperature sensitivity of the lasing threshold current is found to be in good qualitative agreement with observations and with previous reports based on detailed microscopic models. The temperature dependence of the polarization switching point, when the dominant polarization turn off and the orthogonal polarization emerges, is characterized in terms of various model parameters, such as the room-temperature gain-cavity offset, the substrate temperature, and the size of the active region.

© 2008 Optical Society of America

**OCIS codes:** (250.7260) Vertical cavity surface emitting lasers; (260.5430) Polarization; (140.3430) Laser theory

---

## References and links

1. *Vertical-Cavity Surface-Emitting Lasers XII*, C. Lei, and J. K. Guenter, eds., SPIE Proc. vol. 6908, 2008.
2. Y. Suematsu and K. Iga, "Semiconductor lasers in photonics," *J. Lightwave Technol.* **26**, 1132-1144 (2008).
3. S. Mogg, N. Chitica, U. Christiansson, R. Schatz, P. Sundgren, C. Asplund, and M. Hammar, "Temperature sensitivity of the threshold current of long-wavelength InGaAs-GaAsVCSELs with large gain-cavity detuning," *IEEE J. Quantum Electron.* **40**, 453-462 (2004).
4. E. S. Björlin, J. Geske, M. Mehta, J. Piprek, and J. E. Bowers, "Temperature dependence of the relaxation resonance frequency of long-wavelength vertical-cavity lasers," *IEEE Photon. Technol. Lett.* **17**, 944-946 (2005).
5. A. Mircea, A. Caliman, V. Iakovlev, A. Mereuta, G. Suruceanu, C. A. Berseth, P. Royo, A. Syrbu, and E. Kapon, "Cavity mode-gain peak tradeoff for 1320-nm wafer-fused VCSELs with 3-mW single-mode emission power and 10-Gb/s modulation speed up to 70 degrees C," *IEEE Photon. Technol. Lett.* **19**, 121-123 (2007).

6. C. J. Chang-Hasnain, J. P. Harbison, G. Hasnain, A. C. Vonlehmen, L. T. Florez and N. G. Stoffel, "Dynamic, polarization and transverse-mode characteristics of vertical cavity surface emitting lasers," *IEEE J. Quantum Electron.* **27**, 1402-1409 (1991).
7. K. D. Choquette, R. P. Schneider, K. L. Lear and R. E. Leibenguth, "Gain-dependent polarization properties of vertical-cavity lasers," *IEEE J. Sel. Top. Quantum Electron.* **1**, 661-666 (1995).
8. M. B. Willemsen, M. U. F. Khalid, M. P. van Exter, and J. P. Woerdman, "Polarization switching of a vertical-cavity semiconductor laser as a Kramers hopping problem," *Phys. Rev. Lett.* **82**, 4815-4818 (1999).
9. J. Kaiser, C. Degen, and W. Elsässer, "Polarization-switching influence on the intensity noise of vertical-cavity surface-emitting lasers," *J. Opt. Soc. Am. B* **19**, 672-677 (2002).
10. J. Paul, C. Masoller, Y. Hong, P. S. Spencer, and K. A. Shore, "Experimental study of polarization switching of vertical-cavity surface-emitting lasers as a dynamical bifurcation," *Opt. Lett.* **31**, 748-750 (2006).
11. J. Martin-Regalado, F. Prati, M. San Miguel and N. B. Abraham, "Polarization properties of vertical-cavity surface-emitting lasers," *IEEE J. Quantum Electron.* **33** 765-783 (1997).
12. S. Balle, E. Tolkachova, M. San Miguel, J. R. Tredicce, J. Martin-Regalado, and A. Gahl, "Mechanisms of polarization switching in single-transverse-mode vertical-cavity surface-emitting lasers: thermal shift and nonlinear semiconductor dynamics," *Opt. Lett.* **24**, 1121-1123 (1999).
13. M. Sondermann, M. Weinkath, T. Ackemann, J. Mulet and S. Balle, "Two-frequency emission and polarization dynamics at lasing threshold in vertical-cavity surface-emitting lasers," *Phys. Rev. A* **68** 033822 (2003).
14. C. Z. Ning and J. V. Moloney, "Thermal effects on the threshold of vertical-cavity surface-emitting lasers: first- and second-order phase transitions," *Opt. Lett.* **20**, 1151-1153 (1995).
15. T. Rössler, R. A. Indik, G. K. Harkness, J. V. Moloney, and C. Z. Ning, "Modeling the interplay of thermal effects and transverse mode behavior in native-oxide-confined vertical-cavity surface-emitting lasers," *Phys. Rev. A* **58** 3279-3292 (1998).
16. S. F. Yu, W. N. Wong, P. Shum, and E. H. Li, "Theoretical analysis of modulation response and second-order harmonic distortion in vertical-cavity surface-emitting lasers," *IEEE J. Quantum Electron.* **32**, 2139-2147 (1996).
17. P. V. Mena, J. J. Morikuni, S.-M. Kang, A. V. Harton, and K. W. Wyatt, "A comprehensive circuit-level model of vertical-cavity surface-emitting lasers," *J. Lightwave Technol.* **17**, 2612-2632 (1999).
18. H. C. Schneider, A. J. Fischer, W. W. Chow, and J. F. Klem, "Temperature dependence of laser threshold in an InGaAsN vertical-cavity surface-emitting laser," *Appl. Phys. Lett.* **78**, 3391-3393 (2001).
19. C. Degen, I. Fischer, W. Elsässer, L. Fratta, P. Debernardi, G. P. Bava, M. Brunner, R. Hövel, M. Moser, and K. Gulden, "Transverse modes in thermally detuned oxide-confined vertical-cavity surface-emitting lasers," *Phys. Rev. A* **63**, 023817 (2001).
20. Y. Liu, W. C. Ng, K. D. Choquette, and K. Hess, "Numerical investigation of self-heating effects of oxide-confined vertical-cavity surface-emitting lasers," *IEEE J. Quantum Electron.* **41**, 15-25 (2005).
21. C. Chen, P. O. Leisher, A. A. Allerman, K. M. Geib, and K. D. Choquette, "Temperature analysis of threshold current in infrared vertical-cavity surface-emitting lasers," *IEEE J. Quantum Electron.* **42**, 1078-1083 (2006).
22. C. Degen, I. Fischer, and W. Elsässer, "Thermally induced local gain suppression in vertical-cavity surface-emitting lasers," *Appl. Phys. Lett.* **76**, 3352-3354 (2000).
23. J. S. Gustavsson, J. A. Vukusic, J. Bengtsson, and A. Larsson, "A comprehensive model for the modal dynamics of vertical-cavity surface-emitting lasers," *IEEE J. Quantum Electron.* **38**, 203-212 (2002).
24. P. V. Paulau, A. J. Scroggie, A. Naumenko, T. Ackemann, N. A. Loiko, and W. J. Firth, "Localized traveling waves in vertical-cavity surface-emitting lasers with frequency-selective optical feedback," *Phys. Rev. E* **75**, 056208 (2007).
25. L. Spinelli, G. Tissoni, L. A. Lugiato, and M. Brambilla, "Thermal effects and transverse structures in semiconductor microcavities with population inversion," *Phys. Rev. A* **66**, 023817 (2002).
26. C. Masoller, T. Sorrentino, M. Chevrollier, and M. Oria, "Bistability in semiconductor lasers with polarization-rotated frequency-dependent optical feedback," *IEEE J. Quantum Electron.* **43**, 261-268 (2007).
27. F. Prati, P. Caccia and F. Castelli, "Effects of gain saturation on polarization switching in vertical-cavity surface-emitting lasers," *Phys. Rev. A* **66**, 063811 (2002).
28. S. Barland, P. Spinicelli, G. Giacomelli, and F. Marin, "Measurement of the working parameters of an air-post vertical-cavity surface-emitting laser," *IEEE J. Quantum Electron.* **41**, 1235-1243 (2005).

29. E. L. Blansett, M. G. Raymer, G. Khitrova, H. M. Gibbs, D. K. Serkland, A. A. Allerman, and K. M. Geib, "Ultrafast polarization dynamics and noise in pulsed vertical-cavity surface-emitting lasers," *Opt. Express* **9** 312-318 (2001).
30. G. Van der Sande, M. Peeters, I. Veretennicoff, J. Danckaert, G. Verschaffelt, and S. Balle, "The effects of stress, temperature, and spin flips on polarization switching in vertical-cavity surface-emitting lasers," *IEEE J. Quantum Electron.* **42**, 898-906 (2006).
31. A. Homayounfar and M. J. Adams, "Analysis of SFM dynamics in solitary and optically-injected VCSELs," *Opt. Express* **15** 10504-10519 (2007).
32. C. Carlsson, H. Martinsson, R. Schatz, J. Halonen, and A. Larsson, "Analog modulation properties of oxide confined VCSELs at microwave frequencies," *J. Lightwave Technol.* **20**, 1740-1749 (2002).
33. G. Verschaffelt, J. Albert, B. Nagler, M. Peeters, J. Danckaert, S. Barbay, G. Giacomelli, and F. Marin, "Frequency response of polarization switching in vertical-cavity surface-emitting lasers," *IEEE J. Quantum Electron.* **39**, 1177-1186 (2003).
34. C. Degen, I. Fischer and W. Elsässer, "Transverse modes in oxide confined VCSELs: Influence of pump profile, spatial hole burning, and thermal effects," *Opt. Express* **5**, 38-47 (1999)
35. D. M. Grasso and K. D. Choquette, "Temperature-dependent polarization characteristics of composite-resonator vertical-cavity lasers," *IEEE J. Quantum Electron.* **41**, 127-131 (2005).
36. J. Rudolph, S. Döhrmann, D. Hägele, M. Oestreich, and W. Stolz, "Room-temperature threshold reduction in vertical-cavity surface-emitting lasers by injection of spin-polarized electrons," *Appl. Phys. Lett.* **87**, 241117 (2005).
37. M. Holub, J. Shin, D. Saha, and P. Bhattacharya, "Electrical spin injection and threshold reduction in a semiconductor laser," *Phys. Rev. Lett.* **98**, 146603 (2007).
38. G. P. Agrawal and N. K. Dutta, *Semiconductor Lasers*, 2nd ed. Amsterdam, The Netherlands: Kluwer, 1993.

## 1. Introduction

Vertical-cavity surface-emitting lasers (VCSELs) have great potential as inexpensive light sources for high-speed fiber-optical communication systems because they allow direct fiber coupling and provide high beam quality with longitudinal single-mode output power at wavelengths of interest for data links and optical fiber technologies [1, 2].

Much effort has been done towards the development of long-wavelength VCSELs ( $\lambda \geq 1.3 \mu\text{m}$ ), to meet the requirements for communication standards such as 10 Gigabit Ethernet. In contrast to 850 nm VCSELs, that are designed such that the gain peak and the cavity resonance are nearly aligned at room temperature, long-wavelength VCSELs have a relatively large spectral detuning between the gain and the cavity resonance at room temperature. This has the drawback of increased temperature sensitivity, and over the past decade there have been numerous studies devoted to understanding the thermal characteristics of VCSELs, for designing and for optimizing their performance [3, 4, 5].

VCSELs often present polarization instabilities that can be related to variations of the active region temperature with increasing injection current. The output of a VCSEL is usually linearly polarized along one of two orthogonal directions associated with crystalline or stress orientations. When the VCSEL begins to lase, one linear polarization dominates, and when the injection current is increased, in many devices the emission switches to the orthogonal linear polarization [6, 7]. The polarizations, referred to as  $x$  and  $y$ , are associated with the same longitudinal mode, and near threshold, with the same transverse mode. Bistability, hysteresis and stochastic noise-induced switching have been observed near the polarization switching (PS) point [8, 9, 10].

Since the polarizations are split by the material birefringence (the spectral splitting typically being of the order of GHzs), they also have slightly different gains. A thermal mechanism has been proposed for explaining the PS [7]: as the current increases, device heating induces a redshift of both, the gain curve and the optical frequencies of the linear polarizations; however, the gain curve redshifts faster, and there can be a change

of sign of the gain difference between the  $x$  and  $y$  polarizations, causing a polarization switch.

A non-thermal mechanism was proposed within the context of the spin-flip model (SFM) [11]. In this model the  $x$  and  $y$  polarizations are associated with phase-locked states of the two circularly polarized components of the optical field,  $E_{\pm}$ , with a phase difference equal either to 0 or to  $\pi$ . The initial polarization preferred at threshold is determined by the difference in gain-to-loss ratios; however, as the injection current is increased, this difference can be overcome by a change of stability of the phase locked states, resulting in a polarization switch.

In Ref. [12] the SFM model was extended to incorporate a frequency-dependent susceptibility, and thermal effects, which were incorporated through the temperature dependence of the detuning between the cavity resonance and the gain peak. The susceptibility of the quantum-wells (QWs) was described by an analytical expression, which involves a certain number of simplifications, such as low temperature, quasi-equilibrium carrier distributions and parabolic bands. Two types of PS were investigated, occurring when scanning the injection current at constant gain-cavity detuning, and when scanning the detuning at constant injection. The latter was termed thermally induced PS, because an increase of the temperature causes a redshift in different amounts of the cavity resonance and the gain spectrum. The model was employed in [13] to investigate two frequency emission near threshold, where the laser operates in a partially polarized state, giving a good agreement with the experimental observation of anticorrelated dynamics at low frequencies and correlated dynamics on the time scale of relaxation oscillations.

Our approach for incorporating thermal effects in the SFM model differs from that of [12, 13] in two aspects. First, we consider a simpler expression for the QWs susceptibility: the optical gain is assumed to be a Lorentzian in frequency space, and the associated dispersion is represented by the well-known linewidth enhancement factor. Second, we use a rate equation for the active region temperature, proposed in Refs. [14, 15], which allows for a dynamic description of temperature variations, taking into account the decay rate to a fixed substrate temperature, Joule heating, and nonradiative recombination heating. Key parameters of the model are the substrate temperature, the RT gain-cavity spectral detuning, the temperature decay rate, and the active region size.

A main conclusion of our study is that the dependence of the polarization switching point,  $I_{PS}$ , on the substrate temperature,  $T_s$ , and on the RT gain-cavity offset,  $\delta_0$ , is as that of the threshold current,  $I_{th}$ , having both a parabolic-like variation. Higher sensitivity of  $I_{PS}$  to temperature variations is found for parameters corresponding to small birefringence. We also find that the substrate temperature not only modifies the PS point: for sufficiently high temperature, a second PS appears during the thermally driven power-shutoff. With increasing temperature the PS points change, and at a certain temperature, both PSs abruptly disappear. To the best of our knowledge, the occurrence of a second PS near the thermally induced roll-over, and the PS suppression at high enough temperature, have not been reported previously.

In spite of the model simplifications, the dependence of  $I_{th}$  with  $T_s$  and with  $\delta_0$  is found to be in good qualitative agreement with that found using sophisticated models, which take into account the specific structure of the VCSEL, a detailed microscopic calculation of the QWs susceptibility and thermal processes [16, 17, 18, 19, 20, 21]. Thus, another conclusion of our study is that, while a quantitative agreement with the observations can only be achieved by modeling the details of the VCSEL structure and of the QWs susceptibility, a good qualitative understanding can be achieved by using

simpler models.

A limitation of the model proposed here is that it does not take into account spatial effects, because it assumes that the orthogonal linear polarizations are emitted on the fundamental transverse mode. This is particularly important well above threshold, where laser output is emitted in several high-order transverse modes, and Joule heating has been shown to be a dominant mechanism in determining the transverse mode formation [19, 22]. However, the model can be easily extended to incorporate multi-transverse-mode emission, diffusion of carriers and temperature gradients in the active region.

This paper is organized as follows. Section 2 describes the model. First we introduce briefly the original SFM model, and then modify the model to incorporate temperature- and frequency-dependent optical gain, and a rate equation for the temperature of the active region. Results of simulations are presented in Section 3, where we study the dependence of the threshold current,  $I_{th}$ , and of the PS point,  $I_{PS}$ , with respect to various model parameters. The results are compared with experimental observations and numerical simulations previously published in the literature. A summary and a discussion is presented in Section 4.

## 2. Model

### 2.1. Spin-flip model

The four-level spin-flip model describes the optical field in the laser cavity in terms of the slowly-varying complex amplitudes of the two circularly polarized components of the field,  $E_+$ , and  $E_-$ , which multiply carrier waves taken to be of the form  $e^{i\omega_c t}$ , with the reference frequency  $\omega_c$  being that of a longitudinal mode. Because the cavity modes red-shift with the active region temperature,  $\omega_c$  is temperature dependent, as described below.

The complex amplitudes,  $E_+$  and  $E_-$ , are coupled to two carrier populations,  $N_+$  and  $N_-$ , that have opposite spin orientation. The rate equations are [11, 12, 27]:

$$\frac{dE_{\pm}}{dt} = k(1 + i\alpha)(N_{\pm} - 1)E_{\pm} - (\gamma_a + i\gamma_p)E_{\mp} + \sqrt{\beta_{sp}}\xi_{\pm}, \quad (1)$$

$$\frac{dN_{\pm}}{dt} = -\gamma_N(N_{\pm} - \mu + 2N_{\pm}|E_{\pm}|^2) - \gamma_j(N_{\pm} - N_{\mp}). \quad (2)$$

In Eq. (1),  $k$  is the field decay rate [ $\tau_p = 1/(2k)$  being the photon lifetime],  $\alpha$  is the linewidth enhancement factor, and the parameters  $\gamma_a$  and  $\gamma_p$  represent linear anisotropies, dichroism and birefringence respectively. Their effects become clear re-writing Eq. (1) in terms of the linear orthogonal polarization components,  $E_x = (E_+ + E_-)/\sqrt{2}$  and  $E_y = -i(E_+ - E_-)/\sqrt{2}$ ,

$$\frac{dE_{x,y}}{dt} = k(1 + i\alpha)[(N - 1)E_{x,y} \pm inE_{y,x}] \mp (\gamma_a + i\gamma_p)E_{x,y} + \sqrt{\beta_{sp}}\xi_{x,y}, \quad (3)$$

where  $N = (N_+ + N_-)/2$  and  $n = (N_+ - N_-)/2$ . Here one can notice that  $\gamma_a > 0$  ( $\gamma_p > 0$ ) gives the  $x$  polarization higher losses (lower frequency) than the  $y$  polarization. The last term in the r.h.s. of Eqs. (1) and (3) takes into account spontaneous emission noise, with  $\beta_{sp}$  being the noise strength and  $\xi_{\pm}$ ,  $\xi_{x,y}$ , Gaussian white noises.

In Eq. (2),  $\gamma_N$  is the carrier decay rate [ $\tau_N = 1/\gamma_N$  being the carrier recombination time],  $\gamma_j$  is the spin-flip rate, which accounts for the mixing of carrier populations with opposite spin, and  $\mu$  is the pump parameter, which is normalized such that, when  $\gamma_a = 0$  the threshold is at  $\mu_{th} = 1$ .

The model has steady-state solutions that correspond to linearly polarized states,  $x$  and  $y$ , which are associated to phase-locked states of  $E_+$  and  $E_-$ . For the linear polarizations the circularly polarized components have equal amplitudes and frequencies,  $E_{\pm} = E e^{i(\omega t \pm \phi/2)}$ ; the phase difference is either  $\phi = 0$  ( $x$  polarization) or  $\phi = \pi$  ( $y$  polarization); and the carrier densities  $N_+$  and  $N_-$  are balanced ( $N_+ = N_- = N$  and  $n = 0$ ). The frequencies of the linearly polarized solutions, with respect to the reference frequency  $\omega_c$ , are:  $-\gamma_p + \gamma_a \alpha$  ( $x$  polarization) and  $\gamma_p - \gamma_a \alpha$  ( $y$  polarization).

## 2.2. Extended model

In Eqs. (1) and (2) the gain bandwidth is neglected: the gain varies linearly with the carrier density,  $G_{\pm} = gN_{\pm}$ , with the coefficient  $g$ , being equal to 1 because of the normalization of  $N_+$  and  $N_-$ : in the Appendix we show that  $N = (N_+ + N_-)/2$  is the difference between the carrier density and the transparency value, normalized to that difference at threshold [11].

To take into account thermal effects, we need to incorporate a frequency-dependent gain that red-shifts with increasing temperature, and we need to take into account the fact that the cavity mode frequency, that is the reference frequency  $\omega_c$ , also red-shifts with temperature. This can be done by including in Eqs. (1) and (2) a gain coefficient that is frequency and temperature dependent:

$$\frac{dE_{\pm}}{dt} = k(1 + i\alpha)[g(\omega_{\pm}, T)N_{\pm} - 1]E_{\pm} - (\gamma_a + i\gamma_p)E_{\mp} + \sqrt{\beta_{sp}}\xi_{\pm}(t), \quad (4)$$

$$\frac{dN_{\pm}}{dt} = -\gamma_N[N_{\pm} - \mu + 2g(\omega_{\pm}, T)N_{\pm}|E_{\pm}|^2] - \gamma_j(N_{\pm} - N_{\mp}). \quad (5)$$

Here  $\omega_{\pm}$  are the angular frequencies of  $E_{\pm}$ , that can be calculated self-consistently as  $\omega_{\pm} = \text{Im}[\dot{E}_{\pm}/E_{\pm}]$ , and  $T$  is the temperature of the active region.

## 2.3. Optical gain

A lot of research has been done in order to model the optical gain with empirical analytical functions of the carrier density, the emission frequency (or wavelength) and the temperature [17, 23]. Here, for the sake of simplicity, the gain coefficient is approximated by a Lorentzian in the frequency space [24], with the gain peak and the gain bandwidth being temperature dependent:

$$g(\omega, T) = \frac{T_0/T}{1 + [\delta(T) - \omega]^2/\Delta\omega_g^2(T)}, \quad (6)$$

where  $T_0$  is a reference temperature (chosen to be the room temperature);  $\delta(T) = \omega_g(T) - \omega_c(T)$  is the detuning of the gain peak at  $\omega_g$  from the cavity mode at  $\omega_c$ , and  $\Delta\omega_g(T)$  is the gain bandwidth.

The gain peak variation with the active region temperature is given by

$$\hbar\omega_g(T) = \varepsilon_g^0 - \alpha'T^2/(T + \beta), \quad (7)$$

where  $\varepsilon_g^0 = 1.52$  eV,  $\alpha' = 5.405 \times 10^{-4}$  eV/<sup>0</sup>K and  $\beta = 204$  <sup>0</sup>K are typical values for GaAs-based VCSELs [25].

The refractive index is assumed to vary linearly with temperature, at a rate given by  $d\eta/dT$ , and thus the cavity mode frequency,  $\omega_c$ , redshifts with temperature as

$$\omega_c(T) = (2\pi c/\lambda_0)[1 - (1/\eta_0)(d\eta/dT)(T - T_0)], \quad (8)$$

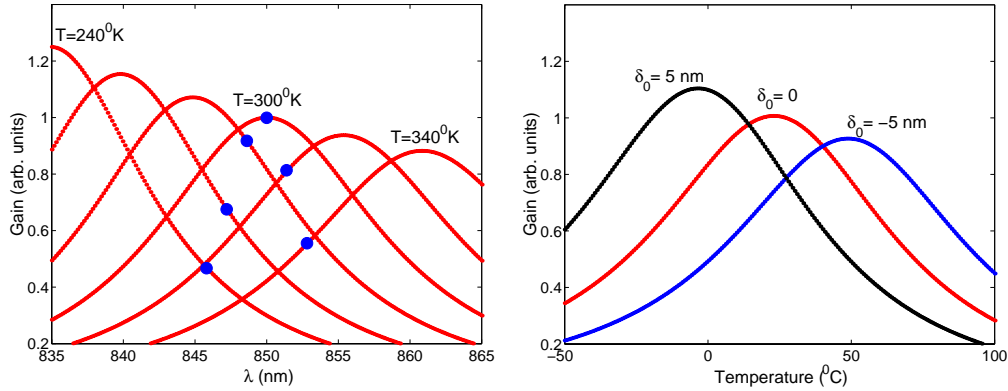


Fig. 1. Left: Gain coefficient vs. wavelength for active region temperature in the range 240 – 340<sup>0</sup> K. The circles indicate the location of the cavity mode. The gain and the cavity mode are aligned at room temperature ( $\delta_0 = 0$  nm). Right: Gain coefficient at the cavity mode vs. temperature of the active region, for three values of the gain-cavity offset at room temperature.

where  $\lambda_0$  and  $\eta_0$  are the wavelength and the refractive index at temperature  $T_0$ . Typical values for VCSELs emitting at  $\lambda_0 = 850$  nm are  $\eta_0 = 3.41$  and  $d\eta/dT = 2.8 \times 10^{-4} \text{ } ^\circ\text{K}^{-1}$  [23]. These parameters result in wavelength variations of  $d\lambda_g/dT \cong 0.27 \text{ nm}/^\circ\text{K}$  and  $d\lambda_c/dT \cong 0.07 \text{ nm}/^\circ\text{K}$  at  $T_0 = 300 \text{ } ^\circ\text{K}$ .

The gain bandwidth is assumed to increase with the square root of temperature [17]:  $\Delta\omega_g^2(T) = \Delta\omega_{g,0}^2(T/T_0)$ , where  $\Delta\omega_{g,0} = 2\pi \times 4 \text{ THz}$ . The parameters for the optical gain model have been chosen such that the plots of the gain coefficient vs. wavelength, and vs. temperature, Fig. 1, are in qualitative good agreement with those obtained from microscopic calculations (see, e.g., Figs. 2(a) and 2(b) of Ref. [21]).

We remark that the optical gain model is valid when the emission wavelength is not too far from the gain peak (about  $\pm 15$  nm), because the gain curves obtained from QWs microscopic theory are rather flat. We verified that the results presented in the next section are robust and independent of the precise shape chosen for the gain curve.

Because we aim at keeping the model as simple as possible, we chose this phenomenological level of description that does not take into account, for example, the asymmetry of the gain curve. The gain asymmetry is particularly important for large gain-cavity offset and can eventually be included in the model, for example, by considering a more refined susceptibility [12], or by considering different shapes for the gain curve in the short and in the long wavelength sides.

#### 2.4. Temperature rate equation

To complete the model we need an equation for the temperature of the active region. We use a phenomenological rate equation [14, 15, 25, 26],

$$\frac{dT}{dt} = -\gamma_T(T - T_s) + \frac{\gamma_N \hbar \omega_c}{c_q} \mathcal{N} + \frac{RS^2}{c_q V_t} \mathcal{J}^2, \quad (9)$$

where the terms in the r.h.s. take into account:

- (i) relaxation to a fixed substrate temperature  $T_s$ , with relaxation rate  $\gamma_T$ .
- (ii) nonradiative recombination with fixed rate  $\gamma_N$ ;  $\mathcal{N}$  is the carrier density and  $c_q$  is the specific heat of the active medium,

(iii) Joule heating, where  $\mathcal{J}$  is the injection current density and  $S$ ,  $V_t$  and  $R$  are the cross section, the total volume, and the total ohmic resistance of the device.

To use this equation we need to relate the carrier and current densities,  $\mathcal{N}$  and  $\mathcal{J}$ , to the dimensionless carrier variable  $N = (N_+ + N_-)/2$  and to the pump parameter  $\mu$  of the spin-flip model. We do this in the Appendix, where we show that

$$N = K(\mathcal{N}/\mathcal{N}_0 - 1), \quad (10)$$

$$\mu = K(\mathcal{J}/\mathcal{J}_0 - 1), \quad (11)$$

where  $K = \tau_p v_g \Gamma a \mathcal{N}_0$  is a dimensionless parameter, with  $v_g$  being the group velocity,  $\Gamma$  the longitudinal confinement factor,  $a$  the differential gain,  $\mathcal{N}_0$  the transparency carrier density, and  $\mathcal{J}_0 = \gamma_N e L_a \mathcal{N}_0$ , the current density needed to achieve transparency, with  $e$  being the electron charge and  $L_a$  the active region thickness. Equations (10) and (11) are as Eqs. (20) and (21) in [27], where gain nonlinearities due to spectral hole burning were incorporated in the SFM model.

Using Eqs. (10) and (11) to substitute  $\mathcal{N}$  and  $\mathcal{J}$  into Eq. (9), we obtain:

$$\frac{dT}{dt} = -\gamma_T(T - T_s) + Z(N/K + 1) + P(\mu/K + 1)^2, \quad (12)$$

where  $Z = \gamma_N \hbar \omega_c \mathcal{N}_0 / c_q$  and  $P = RS^2 \mathcal{J}_0^2 / (c_q V_t)$ . For simplicity, the temperature dependence of  $Z$ ,  $P$ , and  $K$ , and the dependence of  $R$  on the injection current, are neglected.

### 3. Results

We simulated the model equations [Eqs. (4), (5) and (12)] with initial conditions corresponding to transparency:  $\mu = 1$ ,  $N_+ = N_- = 0$ , and  $E_{\pm}$  at the noise level (the real and imaginary parts of  $E_{\pm}$  were set to small random values). The initial value of the substrate temperature was the solution of Eq. (12) at transparency,  $T = T_s + (Z + P)/\gamma_T$ . It should be noticed that, in order to calculate  $dE_{\pm}/dt$  from Eqs. (4), (5), one needs to know  $\omega_{\pm}$  (to calculate the gain), and to calculate  $\omega_{\pm}$ , one needs to know  $dE_{\pm}/dt$ , because  $\omega_{\pm} = \text{Im}[(dE_{\pm}/dt)/E_{\pm}]$ . Thus, we start the simulations with the laser off (at transparency) and chose an initial arbitrary value of  $\omega_{\pm}$ . We verified that the results of the simulations were robust with respect to this initial value. Due to spontaneous emission noise, the frequencies  $\omega_{\pm}$  fluctuate rapidly, and because the active medium has a finite response time, the values of  $\omega_{\pm}$  used to calculate the optical gain, Eq. (6), were averaged over a short time interval (of 0.1 ns). When the laser turns on, the numerical values obtained for  $\omega_{\pm}$  are as those in the original SFM model: when the emission is cw  $x$  polarized  $\omega_{\pm} = -\gamma_p + \alpha\gamma_a$ ; when is  $y$  polarized  $\omega_{\pm} = \gamma_p - \alpha\gamma_a$ . This is due to the fact that the cavity frequency,  $\omega_c$ , is temperature dependent, but the spectral detuning between the linear polarizations and  $\omega_c$  (due to linear cavity anisotropies, represented by the parameters  $\gamma_a$  and  $\gamma_p$ ) is temperature independent.

The parameters used in the simulations are summarized in Table I, and are kept constant unless otherwise stated. For the VCSEL structure and for the parameters of the standard semiconductor laser rate equations ( $\tau_p$ ,  $\tau_N$ ,  $\alpha$  and  $\beta_{sp}$ ) we use the values reported in Ref. [28], where a detailed experimental parameter characterization was performed. Since in [28] polarization and thermal effects were not investigated, other model parameters are estimated in the following way:

1) The linear cavity anisotropies,  $\gamma_a$  and  $\gamma_p$ , are set to values appropriate for studying polarization switching in large and in small birefringent VCSELs. For large birefringence the PS occurs from the high-frequency ( $y$ ) to the low-frequency ( $x$ ) polarization, and

Table 1. Parameters used in the simulations

Value	Parameter	Description
5 $\mu\text{m}$	$R_a$	Device radius
12 ps	$\tau_p$	Photon lifetime [28]
0.5 ns	$\tau_N$	Carrier lifetime [28]
10-70 $\text{ns}^{-1}$	$\gamma_j$	Spin-flip rate (for $T = 10 - 300$ $^{\circ}\text{K}$ )
$\pm 0.4$ $\text{ns}^{-1}$ , 3 – 60 rad/ns	$\gamma_a, \gamma_p$	Anisotropies (dichroism and birefringence)
0.01 $\text{ns}^{-1}$	$\gamma_T$	Temperature decay rate (for $R_a = 5$ $\mu\text{m}$ )
3	$\alpha$	Linewidth enhancement factor [28]
$10^{-4}$ $\text{ns}^{-1}$	$\beta_{sp}$	Spontaneous emission rate [28]
$1.24 \times 10^{18}$ $\text{cm}^{-3}$	$\mathcal{N}_0$	Transparency carrier density [28]
$0.88 \times 10^8$ nm/ns	$v_g$	Group velocity [28]
0.041	$\Gamma$	Longitudinal confinement factor [28]
$1.4 \times 10^{-15}$ $\text{cm}^2$	$a$	Differential gain coefficient [28]
7.5	$K = \tau_p v_g \Gamma a \mathcal{N}_0$	Dimensionless parameter
1.01 mA	$I_0 = e \gamma_N \mathcal{N}_0 V_a$	Transparency current
$1.86 \times 10^6$ J/( $^{\circ}\text{K}\text{m}^3$ )	$c_q$	Specific heat of GaAs [14],[16]
60 $\Omega$	$R$	Device resistance (for $R_a = 5$ $\mu\text{m}$ ) [32]
0.42 $^{\circ}\text{K}/\text{ns}$	$Z = \gamma_N \hbar \omega_c \mathcal{N}_0 / c_q$	Nonrad. recomb. heating coefficient
$1.68 \times 10^{-3}$ $^{\circ}\text{K}/\text{ns}$	$P = RI_0^2 / (c_q V_t)$	Joule heating coefficient (for $R_a = 5$ $\mu\text{m}$ )

has been referred in the literature as type I PS; for small birefringence the PS is from the low-frequency ( $x$ ) to the high-frequency ( $y$ ) polarization, and has been referred to as type II PS. Unless otherwise stated, results are presented for type I PS with parameters  $\gamma_a = 0.4$   $\text{ns}^{-1}$  and  $\gamma_p = 60$  rad/ns.

2) For the spin-flip rate,  $\gamma_j$ , the values employed in the literature vary in a wide range:  $\gamma_j = 10 - 1000$   $\text{ns}^{-1}$  depending on the temperature and on the active region medium [29, 30]. For the sake of simplicity we assume that  $\gamma_j$  varies linearly with the temperature:  $\gamma_j = 10$   $\text{ns}^{-1}$  at  $T = 10$   $^{\circ}\text{K}$ ;  $\gamma_j = 70$   $\text{ns}^{-1}$  at  $T = 300$   $^{\circ}\text{K}$ . We chose this range of values not only because is typically employed in the literature [11, 13, 30, 31], but also, because in this range of  $\gamma_j$  there is polarization switching in a wide region of parameters. A detailed characterization of the influence of  $\gamma_j$  is in progress and will be reported elsewhere.

3) The thermal model parameters [ $\gamma_T$ ,  $c_q$ , and  $R$  in Eq. (9)] are set to values that are consistent with those reported in the literature for GaAs-based VCSELs. For the specific heat,  $c_q$ , references are given in Table I; for the ohmic resistance,  $R$ , values are estimated from Ref. [32], where the differential resistance at 50% of maximum power was found to be in the range 190 – 60  $\Omega$  for VCSELs with aperture diameters of 2 – 10  $\mu\text{m}$ . The temperature decay rate,  $\gamma_T$ , is adjusted to fit experimental measurements of (i) the threshold current,  $I_{th}$ , and (ii) the thermal resistance,  $R_{th}$  [32, 33, 34], which is defined as  $R_{th} = \Delta T / \Delta I$ , where  $\Delta T$  is the temperature rise due to an increase of the injection current  $\Delta I$ . Both,  $I_{th}$  and  $R_{th}$ , depend on the VCSEL size, and in order to fit this dependence, not only the ohmic resistance,  $R$ , but also the temperature decay rate,  $\gamma_T$ , has to decrease with the device size.

Values reported in the literature are in the range  $R_{th} = 15 - 3$   $^{\circ}\text{K}/\text{mA}$  [32, 33] and  $I_{th} = 0.23 - 0.80$  mA [32] for VCSELs with aperture diameters of 2 – 10  $\mu\text{m}$ . The simulations give a variation of  $I_{th}$  and  $R_{th}$  with the device radio, shown in Figs. 2(a) and 2(b), that

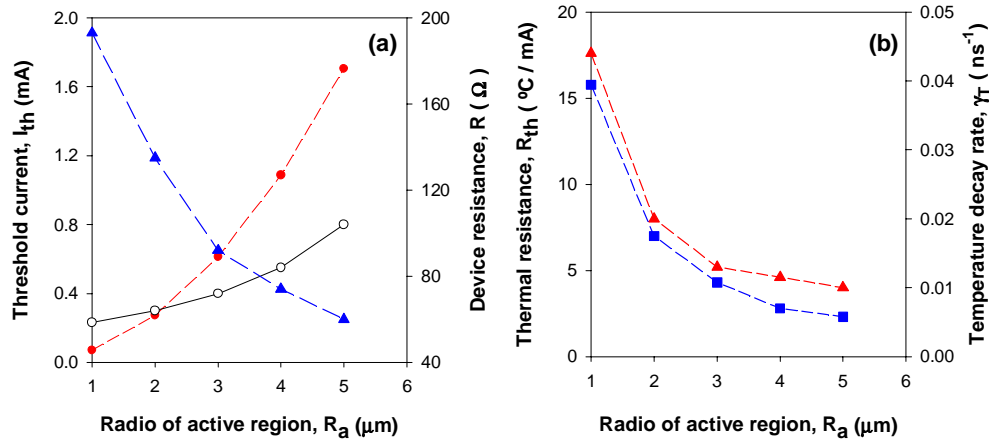


Fig. 2. Left: Variation of the lasing threshold current,  $I_{th}$ , with the radius of active region,  $R_a$ . We compare measurements of [32] (open circles) with results of simulations (dots). The value of the device resistance,  $R$ , is indicated in the right vertical axis (triangles). Right: Thermal resistance,  $R_{th} = \Delta T / \Delta I$ , vs. the active region ratio,  $R_a$  (squares). The value of the temperature decay rate,  $\gamma_T$ , is indicated in the right vertical axis (triangles).

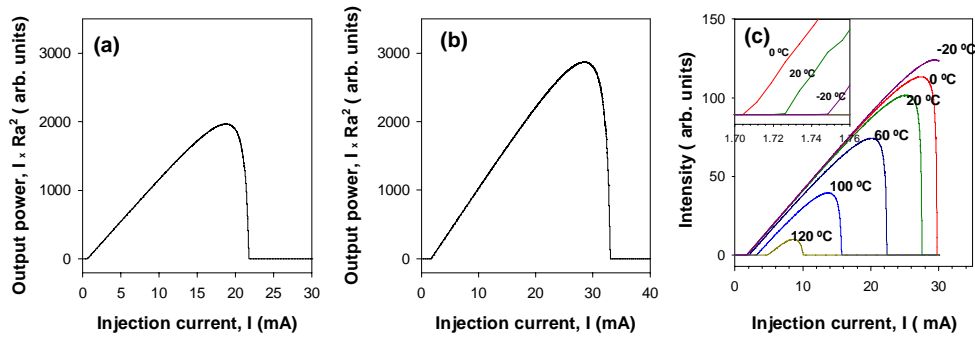


Fig. 3. (a), (b) Dependence of the shape of the LI curve on the active region size. The aperture diameter is  $6 \mu\text{m}$  (a) and  $10 \mu\text{m}$  (b). (c) Variation of the shape of the LI curve with the substrate temperature. The RT gain-cavity offset is  $\delta_0 = -3 \text{ nm}$ . The inset shows a detail of the lasing threshold.

is consistent with these values. The values used for  $R$  and  $\gamma_T$  are indicated in the right vertical axis of Fig. 2(a) and 2(b) respectively. The shape of the LI curve, shown in Fig. 3 for two different aperture diameters, is also consistent with experimental measurements (see Fig. 2 of [34]). We speculate that a better quantitative agreement can be obtained by including in the model spatial effects, such as current leakage, carrier diffusion and temperature gradients.

In Figs. 2 and 3(a), 3(b), the substrate temperature and the RT gain-cavity offset are kept constant ( $T_s = 0^{\circ}\text{C}$  and  $\delta_0 = 0 \text{ nm}$ ). In the following,  $\delta_0$  and  $T_s$  are varied while the device size is kept fixed (results are presented for a  $10 \mu\text{m}$ -diameter VCSEL).

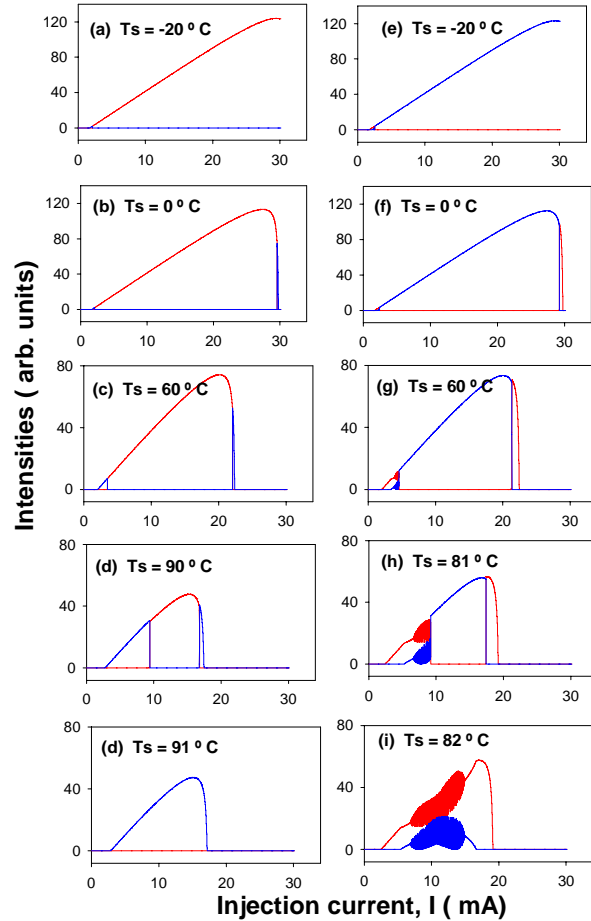


Fig. 4. Polarization-resolved LI curve (x polarization: red; y polarization: blue). The left (right) column is done with parameters corresponding to type I (type II) PS. It can be seen how the substrate temperature,  $T_s$ , affects the PS points: for intermediate  $T_s$ , a second PS appears near the thermally induced power rollover point; at high enough  $T_s$ , both PSs abruptly disappear.

First, let us show that the variation of the thermal roll-over characteristics with the substrate temperature, displayed in Fig. 3(c), is in good qualitative agreement with observations and with simulations of detailed microscopic models (see, e.g., Figs. 17, 19 and 21 of Ref. [17]).

When looking at the polarization-resolved LI curve, Fig. 4, one notices that the substrate temperature not only modifies the lasing threshold and the roll-over characteristics, but also the PS points. For low temperature only one PS occurs and no roll-over behavior is seen (the LI relation is linear until the laser abruptly switches off). At an intermediate temperature a second PS appears during the thermally driven power-shutoff. As  $T_s$  increases the two PS points move, and at a critical temperature both PSs abruptly disappear.

A polarization switching occurring when the total output power starts to decrease was observed experimentally in [35]; it was also observed the suppression of this PS

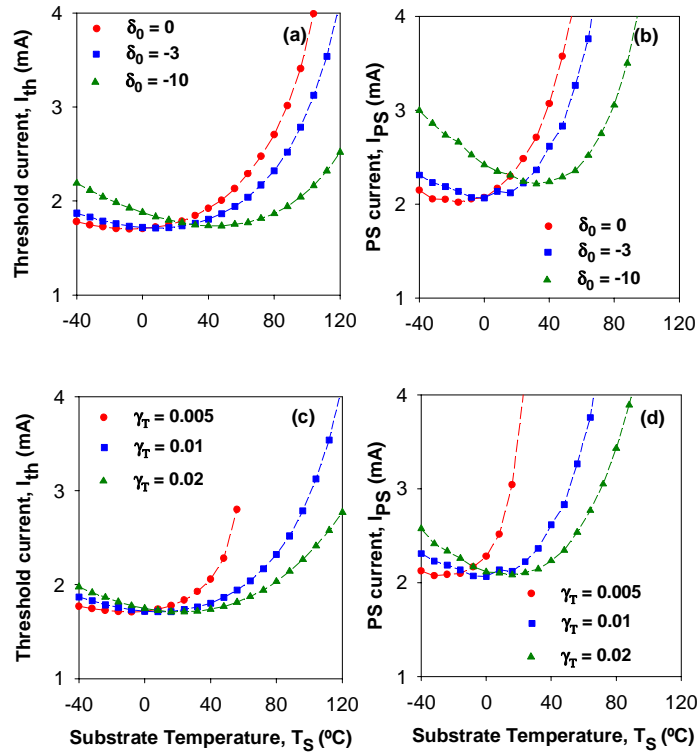


Fig. 5. Threshold current (a) and polarization-switching current (b) versus the substrate temperature for  $\gamma_T = 0.01 \text{ ns}^{-1}$  and various values of the RT gain-cavity offset,  $\delta_0$  (in nm). Threshold current (c) and polarization-switching current (d) versus the substrate temperature for  $\delta_0 = -3 \text{ nm}$  and various values of the temperature decay rate,  $\gamma_T$  (in  $\text{ns}^{-1}$ ).

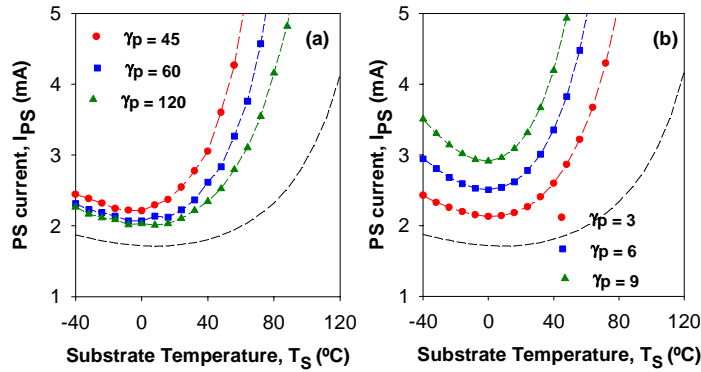


Fig. 6. Influence of the birefringence parameter,  $\gamma_p$ . Polarization-switching current for type I PS (a) and for type II PS (b) versus the substrate temperature for fixed RT gain-cavity offset,  $\delta_0 = -3 \text{ nm}$ , and various values of  $\gamma_p$  (in  $\text{rad/ns}$ ). The dashed lines show the threshold current, that does not depend on  $\gamma_p$ .

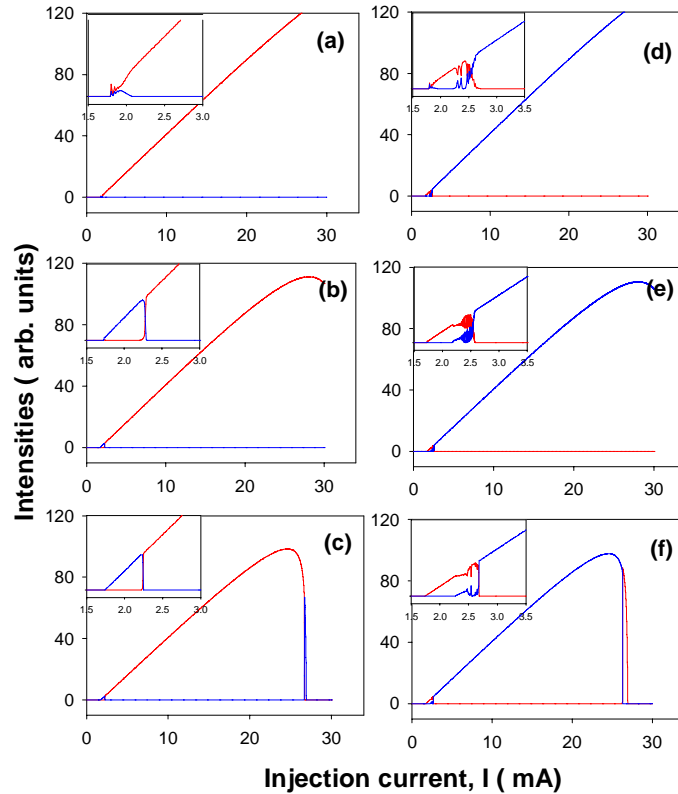


Fig. 7. Dependence of the polarization-resolved LI curve on the duration of the current ramp. The injection current increases linearly in 1000 ns (a), (d) 5000 ns (b), (e) and 50000 ns (c), (f). The left (right) column is done with parameters corresponding to type I (type II) PS. The insets show a detail of the LI curve. The gain-cavity offset is  $\delta_0 = -3$  nm, and the substrate temperature,  $T_s = 25^\circ\text{C}$ .

for sufficiently high substrate temperature. However, the structure of the device investigated in [35] is different from that considered here: it consists of a monolithic composite-resonator vertical-cavity laser composed of three distributed Bragg reflectors that separate two identical optical cavities. To the best of our knowledge, in conventional VCSELs, the occurrence of a second PS near the thermally induced power roll-over, and the PS suppression at high enough temperature, have not been reported before. In [35], the mechanism causing the PS in the region of the thermal roll-over was interpreted as due to increased absorption (caused by self-heating effects); and the PS suppression at high enough substrate temperature, as due to decreased absorption at longer wavelengths (the gain and cavity resonance both shift to longer wavelengths, but the gain shifts faster). Here, we interpret the appearance of a second PS during the power roll-over, and the PS suppression at high temperature, in a similar way, as caused by temperature-induced changes in the different gain-to-loss ratios of the two polarizations.

The variation of the lasing threshold current,  $I_{th}$ , with the substrate temperature is displayed in Fig. 5(a), for various values of  $\delta_0$ . The parabolic-like dependence of  $I_{th}$  is also in good agreement with observations and with simulations reported in the literature (see, e.g., Figs. 1 and 3 of Ref. [21]). The injection current at which the PS occurs,  $I_{PS}$ ,

also presents a parabolic-like dependence with  $T_s$ , as shown in Fig. 5(b).

The influence of the temperature decay rate,  $\gamma_T$ , is shown in Figs. 5(c) and 5(d), where  $I_{th}$  and  $I_{PS}$  are plotted vs.  $T_s$  for fixed gain-cavity offset and various values of  $\gamma_T$ . Small  $\gamma_T$  results in VCSELs with reduced temperature sensitivity. The influence of the birefringence parameter,  $\gamma_p$ , is presented in Fig. 6, where is observed that the temperature sensitivity is larger for small  $\gamma_p$ , the parabolic variation being more pronounced.

Finally, let us discuss the effect of the speed of the current ramp. Previous figures were all done with the injection current varying linearly from the transparency value, 1 mA, to 30 mA in a time interval  $\Delta T = 20000$  ns. As shown in Fig. 7, with a much faster ramp thermal effects do not play a significant role, as there are no differences with simulations of the original SFM model. Thermal effects play a role with a slow current ramp: the slower the ramp, the sooner and the more abruptly the laser switches off.

#### 4. Summary and Conclusions

We proposed a modification of the spin-flip model, which incorporates thermal effects in a simple and computationally efficient way, allowing for a dynamic description of temperature variations. The model includes a rate equation for the active region temperature, which takes into account the decay rate to a fixed substrate temperature, Joule heating, and nonradiative recombination heating. The model also takes into account the thermal red-shift of both, the gain peak and the cavity resonance. Spatial effects such as carrier diffusion and temperature inhomogeneities were neglected, but can be easily incorporated in the model.

The dependence of the lasing threshold and of the shape of the LI curve on various model parameters, despite the strong simplifications of the model, is in good qualitative agreement with results obtained from simulations of models that take into account the detailed VCSEL structure, as well as microscopic light-matter interactions.

We found that the dependence of the polarization switching point,  $I_{PS}$ , on the substrate temperature,  $T_s$ , and on the RT gain-cavity offset,  $\delta_0$ , is parabolic-like, similar to that of the threshold current,  $I_{th}$ , for both types of PS (for small and for large birefringence). Higher temperature dependence of the PS point was observed for small birefringence. In the high temperature region we found that the PS can be completely suppressed, while for intermediate temperatures, a second PS can occur during the thermally induced power switch off. To the best of our knowledge, this behavior has not yet been observed and we hope that our results will stimulate further studies.

Our model can also be employed to investigate the polarization properties of the novel spin-VCSELs [36, 37], that demonstrate an impressive threshold reduction at room temperature in commercial VCSELs by the injection of spin-polarized electrons. In these devices the spin relaxation time is a key parameter, and a detailed characterization of the influence of the temperature dependence of the spin-flip rate is important; this study is in progress and will be reported elsewhere.

#### Appendix

Here we derive Eqs. (10) and (11), relating the dimensionless quantities  $N = (N_+ + N_-)/2$  and  $\mu$  of the spin-flip model, to the carrier and injection current densities,  $\mathcal{N}$  and  $\mathcal{J}$ , of the temperature rate equation.

First, we assume that the optical field is linearly polarized (e.g., along the  $x$  direction:  $E_x = E$ ,  $E_y = 0$ ,  $N_+ = N_- = N$  and  $n = 0$ ). Neglecting cavity anisotropies ( $\gamma_a$  and  $\gamma_p$ ) and

noise, from Eqs. (1) and (2) we obtain

$$dE/dt = k(1 + i\alpha)(N - 1)E, \quad (13)$$

$$dN/dt = -\gamma_N(N - \mu + N|E|^2). \quad (14)$$

Next, we compare with the usual single-mode semiconductor laser equations, which in their simplest form are [38]:

$$d\mathcal{E}/dt = (1/2)(1 + i\alpha)[v_g\Gamma a(\mathcal{N} - \mathcal{N}_0) - 1/\tau_p]\mathcal{E}, \quad (15)$$

$$d\mathcal{N}/dt = \mathcal{J}/(eL_a) - \gamma_N\mathcal{N} - v_g\Gamma a(\mathcal{N} - \mathcal{N}_0)|\mathcal{E}|^2, \quad (16)$$

where  $\mathcal{E}$  is optical field,  $\mathcal{N}$  is the carrier density,  $\mathcal{N}_0$  is the carrier density at transparency,  $\tau_p = 1/(2k)$  is the photon lifetime,  $v_g$  is the group velocity,  $\Gamma$  is the longitudinal confinement factor,  $a$  is the differential gain,  $\mathcal{J}$  is the injection current density,  $e$  is the electron charge and  $L_a$  is the active region thickness.

Comparing (15) with (13) we obtain

$$N = \tau_p v_g \Gamma a (\mathcal{N} - \mathcal{N}_0). \quad (17)$$

The threshold condition is given by

$$v_g \Gamma a (\mathcal{N}_{th} - \mathcal{N}_0) = 1/\tau_p, \quad (18)$$

and using Eq. (17) we see that:

$$N = (\mathcal{N} - \mathcal{N}_0)/(\mathcal{N}_{th} - \mathcal{N}_0), \quad (19)$$

i.e.,  $N$  is the difference between the carrier density and the transparency value, normalized to that difference at threshold [11, 28, 27].

Comparing (16) and (14) and using (17) we obtain:

$$\mu = \tau_p v_g \Gamma a [\mathcal{J}/(eL_a \gamma_N) - \mathcal{N}_0]. \quad (20)$$

Defining  $K = \tau_p v_g \Gamma a \mathcal{N}_0$  and  $\mathcal{J}_0 = eL_a \gamma_N \mathcal{N}_0$ , (17) and (20) can be simplified to

$$N = K(\mathcal{N}/\mathcal{N}_0 - 1) \quad (21)$$

$$\mu = K(\mathcal{J}/\mathcal{J}_0 - 1). \quad (22)$$

## Acknowledgment

This research was supported by U.S. Air Force Office of Scientific Research under grant FA9550-07-1-0238. CM acknowledges support from the ‘‘Ramon y Cajal’’ Program (Spain) and the Spanish Ministerio de Educacion y Ciencia through project FIS2005-07931-C03-03. MST acknowledges support of CONICET grant PIP 6474, FONCyT grant 3/09598.